DOE/ER/82909-1

Final Technical Report

DoE Grant No.: DE-FG02-99ER82909

Title: "Low-Cost, High-Resolution and High-Sensitivity PET Detector Modules"

The above grant was a Phase I SBIR grant. A follow-up Phase II SBIR grant application was submitted on March 31, 2000. Attached please find 17 pages from that application which detail the technical results achieved during the Phase I effort.

A brief summary of what was attempted and achieved would be as follows:

- Positron Emission Tomography (PET) imaging could benefit from a low-cost, high-performance sensor – we began with some proof-of-concept sensor modules and within the Phase I Effort designed and tested new readout electronics making use of a new (single-photon counting readout) technique.
- Our purpose was to test whether PET detector modules incorporating wavelength-shifting fiber and single-photon counting electronics readout would have sufficiently high spatial resolution (and sufficiently low cost) for the envisaged PET imaging applications.
- The tests showed that the spatial resolution achieved was limited by intrinsic properties of the sensor (in particular, detector Compton scattering) rather than the readout electronics.
- The single-photon-counting electronics method proved feasible, but ultimately it had no significant cost or performance benefits relative to more conventional methods, which might be described as "temporally integrated photon measurement electronics" to distinguish from the above.
- We had originally envisaged application of this technology to a single-organ imaging system (e.g. instrumentation for Positron Emission Mammography) or to small animal imaging systems. For these systems high spatial resolution is critical, and the low-cost imperative is lessened because of overall lower system costs.
- The types of methods pioneered here have continued to prove viable for low-cost, whole-body PET imaging instrumentation. The scope of the effort required to establish a commercially viable form of this technology was beyond the capacity of Tomotronics, Inc. PhotoDetection Systems, Inc., was later established with some of the former principals of Tomotronics as co-founders, and due to its considerably more stable financing has carried forth development of cost-effective PET instrumentation using wavelength-shifting fiber readout to the present day (May, 2005).
- Other principals from Tomotronics later joined PEM Technologies, which later changed its name to NaviScan, and there they have successfully produced high-spatial resolution Positron Emission Mammography instrumentation using an alternative sensor (different crystal, no wavelength-shifting fiber) and dedicated readout electronics.

DOE Patent Clearance Granted

MP Dvorscak July 5 2005

Mark P. Dvorscak Date
(630) 252-2393
E-mail: mark.dvorscak@ch.doe.gov
Office of Intellectual Property Law
DOE Chicago Operations Office

DISCLAIMER

This report was prepared as an account of work sponsored by an agency of the United States Government. Neither the United States Government nor any agency Thereof, nor any of their employees, makes any warranty, express or implied, or assumes any legal liability or responsibility for the accuracy, completeness, or usefulness of any information, apparatus, product, or process disclosed, or represents that its use would not infringe privately owned rights. Reference herein to any specific commercial product, process, or service by trade name, trademark, manufacturer, or otherwise does not necessarily constitute or imply its endorsement, recommendation, or favoring by the United States Government or any agency thereof. The views and opinions of authors expressed herein do not necessarily state or reflect those of the United States Government or any agency thereof.

DISCLAIMER

Portions of this document may be illegible in electronic image products. Images are produced from the best available original document.

5. Degree to which Phase I has Demonstrated Technical Feasibility –

Purpose, Scope, and Objectives of Phase I Effort

Our Phase I Technical Abstract's description of the overall objective of our Phase I and II projects states:

"We propose to build high-performance PET detector modules using relatively inexpensive materials combined in an unconventional and innovative manner. In particular, we will use wavelength-shifting optical fiber readout of CsI(Na) scintillator plates. Our goal is to produce devices with very high spatial resolution and depth-of-interaction sensitivity for uniformly high resolution across an extended field of view. Within the scope of this project, our emphasis will be on obtaining high resolution, large acceptance and high sensitivity at low cost".

We stand by this statement. Our Phase I "Identification and Significance of Problem/Opportunity" has also withstood the test of time, with the exception of its final paragraph. In this paragraph we stated:

"Our business strategy does not call for immediately implementing our technical approach within a large-field tomograph. Instead, it calls for initial cost-effective success in high-performance systems with a limited field of view [such as] small animal imagers [and] single-organ imagers."

Our business strategy has now changed for several reasons. We are now convinced that the combination of increasing market demand and the unique capabilities of our technology call for addressing the whole-body PET scanner market. The market for these devices is considerably larger and more established than the market for small animal and single-organ PET imagers. Our business plan was guided by results from our Phase I program, as anticipated in a section of our Phase I proposal entitled "Application of Results to System Design":

"Based on results of the above tasks, designs will be generated which optimize the price/performance trade-offs of WLSF-PET readout using single-photon counting to both very high-resolution, limited-field applications (e.g. animal imagers, breast imagers, etc.) and to high-resolution, large-field applications (e.g. "zoom lens", *dedicated PET ring* [emphasis added], etc.). The results of the optimization will be used to guide Tomotronics' business strategy and to inform our decisions relating to product development direction and Phase II proposal content."

We have explicitly fulfilled each of our Phase I objectives, as will be detailed in the following sections. As listed in the "Performance Schedule" of our Phase I proposal, these objectives were:

- Objective 1: Design and implementation of proof-of-concept prototype electronics for the photon-counting readout of existing WLS fiber prototype PET detector modules.
- Objective 2: Characterization of the performance of existing wavelength-shifting fiber prototype PET detector modules when outfitted with photon-counting readout electronics.
- Objective 3: Application of the results of the above tasks to the design, optimization, and anticipated cost/performance analysis of wavelength-shifting fiber PET detector modules. systems.

As our product focus has evolved, so has our understanding of several issues relating to device optimization and demonstration of technical feasibility. In particular, much of the original motivation for the introduction of photon-counting electronics was the need for extremely high spatial resolution in small animal or single organ imaging. While spatial resolution remains an important performance parameter for a whole-body PET scanner, there is no need for spatial resolution beyond the statistical limits imposed by accumulated count statistics. For a whole-body PET scanner, count statistics are determined by system sensitivity and rate capability, plus patient dose and scan time. The highest-resolution commercial whole-body PET scanners have at best 4mm FWHM spatial resolution at the center of the field-of-view, degrading to >5mm FWHM at >10cm from the center. We plan our device to have <4mm FWHM resolution uniformly throughout the field of view, and have designed the instrument to collect sufficient event statistics to take advantage of this high resolution. In this context, the principal advantages of photon-counting readout are its low cost, high speed, and especially its potential for high system rate capability. We have built and characterized photon-counting readout circuits and outfitted prototype PET detector modules with them. The technical feasibility of a system incorporating these modules has been assessed in pursuit of our third objective, which has elucidated the connection between module-level response and system-level performance.

Summary of Results of Phase I Effort:

Our Phase I Research Project demonstrated:

- That photon-counting readout electronics provide an accurate and cost-effective method for reading out temporally distributed low light-level signals from multianode photomultipliers.
- That photon-counting readout of wavelength-shifting fiber/scintillator PET modules gives accurate gamma photon interaction coordinate information in 3 dimensions.
- That incorporation of wavelength-shifting fiber/scintillator PET modules with photon-counting readout into a whole-body PET detector system is expected to result in a system with performance that meets or exceeds that of the best current commercial PET systems, at a lower cost.

We have therefore directly demonstrated feasibility for our technology at the module level, and have projected feasibility for our technology at the system level through simulation. After a review of the technical basis of our new technology, the results obtained in pursuit of each of our Phase I objectives is detailed below.

Details of Phase I Accomplishments – Introduction:

We have designed and implemented a set of electronics utilizing single-photon counting for the readout of PET detector modules using a wavelength-shifting fiber-based design. The goal of this effort was to demonstrate the feasibility of this method for reducing the cost of the wavelength-shifting fiber detector design while improving its performance. The motivation behind the wavelength-shifting fiber-based (WLSF) PET detector module design is to provide high-performance PET capabilities at low cost, by combining inexpensive materials with novel electro-optical readout techniques. We expect the ~~single-photon~~ photon counting readout method to reduce system costs for WLSF-PET modules by reducing the number of multi-anode photomultipliers needed to read out the WLSF-PET modules without degrading system performance, and by reducing the cost of readout electronics for these multi-anode PMTs. We expect the ~~single-photon~~ photon counting readout method to improve spatial resolution and other performance attributes of WLSF-PET modules by lessening the effects of stray light and of random low-energy coincidences at high rates, and optionally by lessening the effects of Compton scattering within the WLSF-PET detector modules. The capabilities of a WLSF-PET system with ~~single-~~photon counting readout were experimentally demonstrated by combining our new readout electronics with WLSF-PET detector modules which had previously been constructed at the Boston University Center for Photonics.

A basic understanding of the operating principles of WLSF-PET detector modules is important for understanding our readout electronics design, and for understanding the potential of the combined system. In what follows we will briefly summarize a more complete description which was published as "First Results with High-Resolution PET Detector Modules using Wavelength-Shifting Fibers", *IEEE Trans. Nucl. Sci.* 45:2993-2999, 1998, a copy of which is attached. Figure 1 schematically illustrates the optics of a WLSF-PET detector module. For flat polished crystals, total internal reflection guides scintillation light emitted at shallow angles with respect to the crystal surface toward the crystal edges. Light emitted nearly normal to the surface exits the crystal above and below the gamma ray interaction point (assuming a photocapture event for the moment). This exiting light position may be sensed locally by inexpensive wavelength-shifting (fluorescent) plastic optical fibers, which absorb primary scintillation photons and isotropically re-emit secondary photons at longer wavelengths.

Perpendicular fiber ribbons (X-fibers and Y-fibers) on opposite sides of a thin, polished crystal layer may thus be used to measure gamma-ray interaction positions in two dimensions. Further fibers at the edges of crystal layers (Z-depth fibers) may be used to sense scintillation light which was totally internally reflected within a layer, providing information on depth-of-interaction within a multilayer stack. Alternatively, one may read out fiber ribbons from different depths within a multilayer stack with different photosensors, such as the separate anodes of a multianode photomultiplier. Within a wavelength-shifting fiber, a small fraction of the secondary photons emitted at angles near that of the fiber axis are piped to fiber readout photosensors, while most emerge transversely from the fibers and traverse both scintillator and fibers within a multilayer stack transparently. This unpiped light can be collected with a standard Anger array on the module surface to provide energy and trigger information as well as approximate interaction coordinates. This technique decouples energy and timing (Anger) functions from position determination (fiber) functions.

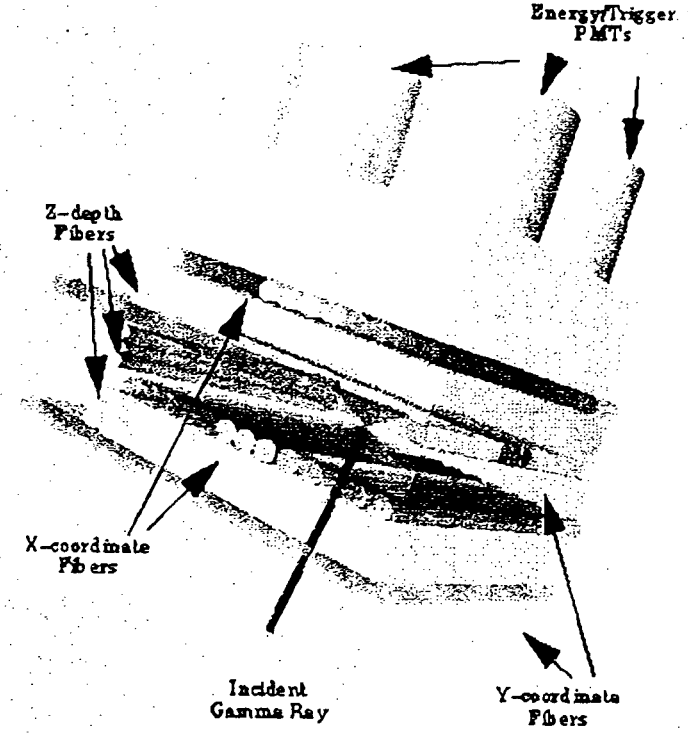

Fig 1 : 3D Illustration of prototype detector

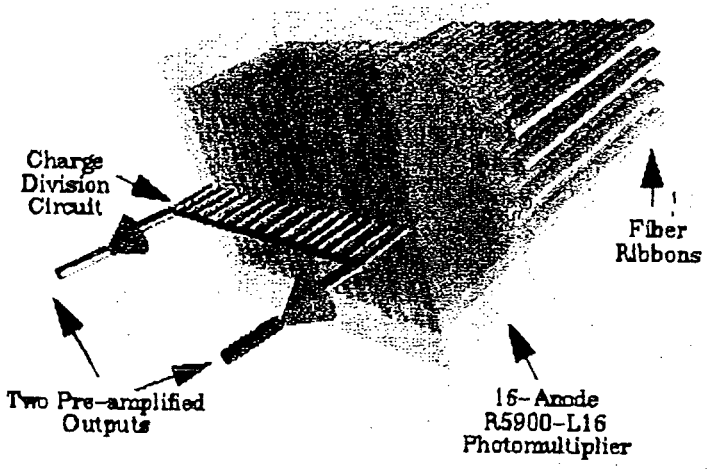

Fig 2 : 3D Illustration of Fiber Readout Method

Multiplexed coupling of wavelength-shifting fiber ribbons to multianode PMTs is essential for cost-effectiveness in the WLS-PET design, but it can introduce errors and degrade system spatial resolution if implemented improperly. In the first generation WLS-PET detectors which have been implemented by BU Photonics group, readout of multianode PMTs was based on charge division (as shown in figure 2). In charge-division readout, two ends of a resistor network connecting the anodes are coupled to ADCs for readout, with the ratio of the charges collected from the two network ends encoding the light collection position (the sum of the collected charge is proportional to the number of photoelectrons collected). Since the converted photons from all fiber ribbons combined at a given multianode PMT are spatially distributed, this method effectively measures the centroid of this spatial distribution. Unfortunately, distribution centroid measurements are sensitive to the presence of outliers, which in this case result from the presence of "stray" or "background" photons in addition to those clustered near the peak of the distribution. These additional photons, which in most cases make up a small fraction of the total but which are widely distributed spatially, can arise from a number of causes, including:

- Scintillation photons which are incident on the polished crystal surface at oblique angles but which are too normal for total internal reflection may be Fresnel reflected (in a polarization-dependent manner) a few times before escaping into the fibers.
- Totally-internally-reflected scintillation photons may escape from the crystal if they scatter at an imperfectly-polished crystal surface.
- Scintillation light totally-internally-guided to the crystal edges may reflect into top or bottom (rather than edge) WLS ribbons and be fluorescently converted there.
- Some scintillation photons (particularly at longer wavelengths) exiting the polished crystal normally will pass entirely through the nearest fiber ribbon but be absorbed and fluorescently converted when they encounter a later fiber ribbon within the stack.
- Compton scattering within the detector modules can lead to more than one position where scintillation light is produced within the stack, with these positions then superimposed during multiplexed fiber readout.
- Pile-up of random coincidences between true events and random singles elsewhere in the detector module may be superimposed through multiplexed readout.

The fact that the BU Photonics group was able to obtain 3mm FWHM spatial resolution from prototype WLSF-PET modules despite all the above effects indicates that their combination is not overwhelming, although it is troublesome. However, the greater the degree of multiplexing (and the higher the event rate) the more pronounced these effects become. With the multianode PMTs a major cost-driver for the system, one cannot cost-effectively use more of them and leave their photosensitive readout areas underpopulated. Single-photon counting provides a solution to the above dilemma by achieving the cost-effective readout of a large number of independent anodes from a multianode PMT, rather than combining signals optically at the PMT face or combining them electrically through resistively coupled charge division signals. In our design we individually discriminate anode signals from individual photoelectrons to provide temporally narrow pulses, and use Programmable Logic Devices (PLDs) to count the number of pulses on each anode within a time window analogous to an ADC gate. The result measures entire photon spatial distributions, rather than just the means of these distributions, leading to better resolution even with fully filled multianode PMTs.

Hamamatsu's compact metal channel photomultipliers were selected for this application because of their relatively low cost per anode signal and their spatial compactness in comparison with discrete photomultipliers. These devices come in two distinct types. The first type is position-sensitive PMTs that use crossed-wire anodes and which are typically read out with 1- or 2-dimensional charge division (e.g. R7600-C8, R7600-C12). The second type is true multianode PMTs, with separate readout signals corresponding to distinct photocathode input regions, where these anode signals are typically read out individually (e.g. R5900-L16, R5900-M16, R5900-M64). Our future PET modules call for R7600-C12 PMTs, which use 12 crossed anode wires (6 x-wires and 6 y-wires) to provide position-sensitive information across a roughly 22mm x 22mm photocathode region. As will be discussed in more detail below, we use temporal coincidences between x- and y- wire single photon signals to provide 36 channels of photon counting from a single R7600-C12 PMT. This provides the lowest cost per digitization channel of any of the available alternatives. Our earlier WLSF-PET prototype modules were, however, implemented with R5900-L16 PMTs. Rather than retrofit the prototype modules to use new R7600-C12 PMTs (and re-route their fibers), we opted to produce a second set of photon-counting electronics appropriate for the older R5900-L16 PMTs. While our future implementations will use fewer R7600-C12's to reduce costs, our current implementation uses a relatively large number of R5900-L16 PMTs per module, giving us additional information on module performance.

Objective 1: Proof-of-concept Prototype Electronics

We first implemented a set of 36 4-bit counters within two PLDs which we used to read out a single R7600-C12 PMT. Each counter was reset at the time of the gate's leading edge. At the end of the gate the data from several 4-bit counters were gathered and transferred through a 32-bit parallel bus and PCI interface. We used Tomotronics' custom PCI interface, which is capable of 100 Mbyte/s data transfers, to read out the data through a PC. Figure 3 shows a photograph of the PMT interface board developed for the R7600-C12. The R7600-C12 operating voltage is typically about 800V, and we provide both a high-voltage divider circuit and photon counting electronics on the same circuit board. Each of the 12 anode signals is separately amplified and fed to a fast CMOS comparator (MAX964, Maxim Semiconductors) which discriminates analog signals above a fixed threshold of 8-10 mV and generates corresponding TTL logic signals. A common discriminator threshold was used for all of the X- and Y-anode wires. The output of each discriminator channel was next fed to one of two programmable logic devices (PLDs) – we have selected Altera EPM7128S PLDs based on their cost-effectiveness, number of available input pins, and internal logic resources. The readout of a single R7600-C12 PMT requires two PLDs, with each detecting and counting coincidences on 3 x 6 anode input wire combinations. For each possible combination of X- and Y-anode input wires, a PLD was programmed as a 4-bit counter to count coincidences between 10ns-wide discriminator outputs which occur during a externally-generated digitization time window (i.e. external gate).

In addition to photon-counting readout electronics, we implemented a second set of readout electronics which used 12 ADC channels to read out a given R7600-C12 PMT through the same PCI interface that we used for photon counting readout. The same external gate could be used with either the ADC readout or the photon counting readout, and comparison of results using the two readout methods allowed us to distinguish effects due to PMT characteristics from those due to the characteristics of the photon counting electronics. We first illuminated each R7600-C12 PMT with light from a blue LED that provided a 2mm diameter spot at the PMT window. The LED and optical collimator were attached to a support structure which was mounted to a computer-controlled XY scanning table, so that the light spot could be scanned across the PMT input window. Each scan was performed on a 12 by 13 grid with 2mm pitch in each direction, with 3000 light pulses used per grid point. The light level from the LED was set to provide ~20 photoelectrons per pulse, as seen from the ratio of the collected charge to the average charge collection for single photoelectrons. For each of the anode wires, the ADC data was then used to determine the variation in PMT charge output as a function of light spot incident position.

All R7600-C12 PMTs evaluated showed appreciable gain non-uniformity, differing by as much as a factor of 2 in gain between their highest gain and lowest gain regions. Most tubes demonstrated fair uniformity (+-30%) over about 75% of their input area, combined with considerably higher gain in the remaining 25%. The high-gain region was typically along one of the edge-most wires, as illustrated in Figure 4. This figure shows the average ADC output as a function of position along each of the 6-x and 6-y anode wires, for input positions that were centered over each of the wires. Although separate thresholds for each of the anode wires may have helped our photon counting uniformity somewhat, it is evident that gain variations along the anode wires ultimately limit the efficiency uniformity for photon counting with an R7600-C12. ADC readout of R5900-L16 PMTs with our scanner set-up showed these PMTs to be much more uniform.

After characterizing several R7600-C12 PMTs in terms of gain variation as a function of position, we evaluated these devices further with photon counting readout. Each PMT was scanned with photon counting readout using the same 12 x 13 grid as with ADC readout, but with a total LED illumination of about 5 photoelectrons as measured with the ADCs. For each event, the output of each of the 6 x 6 x-y coincidence photon counters were recorded and the results histogrammed. From these histograms, we determined the location and extent of the sensitive region on the photocathode corresponding to each of the x-y coincidence photon counters, and the relative efficiency of each of these counters for each source position. The result of a typical scan is shown in Figure 5. Since the LED output was set to a constant level for the scans described above, we were able to measure the relative efficiency of the photon counting channels by comparing their relative counting rates when the LED was illuminating each channel's maximally sensitive region at the PMT window. At the same maximally sensitive illumination points, we were then able to use ADC readout to measure the number of photoelectrons as determined by the ratio of the average charge collected to the average charge collected from single photoelectrons. We then compared the number of photoelectrons as seen with the ADC readout to those seen with the photon counting readout.

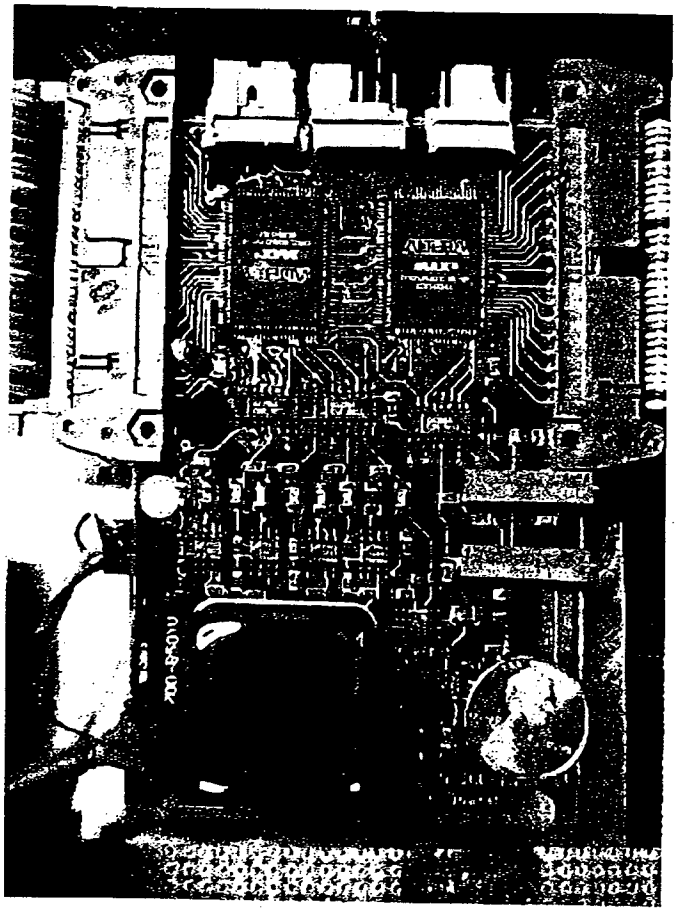

Figure 3: Photon Counting Electronics Board Implemented for R7600-C12 PMT

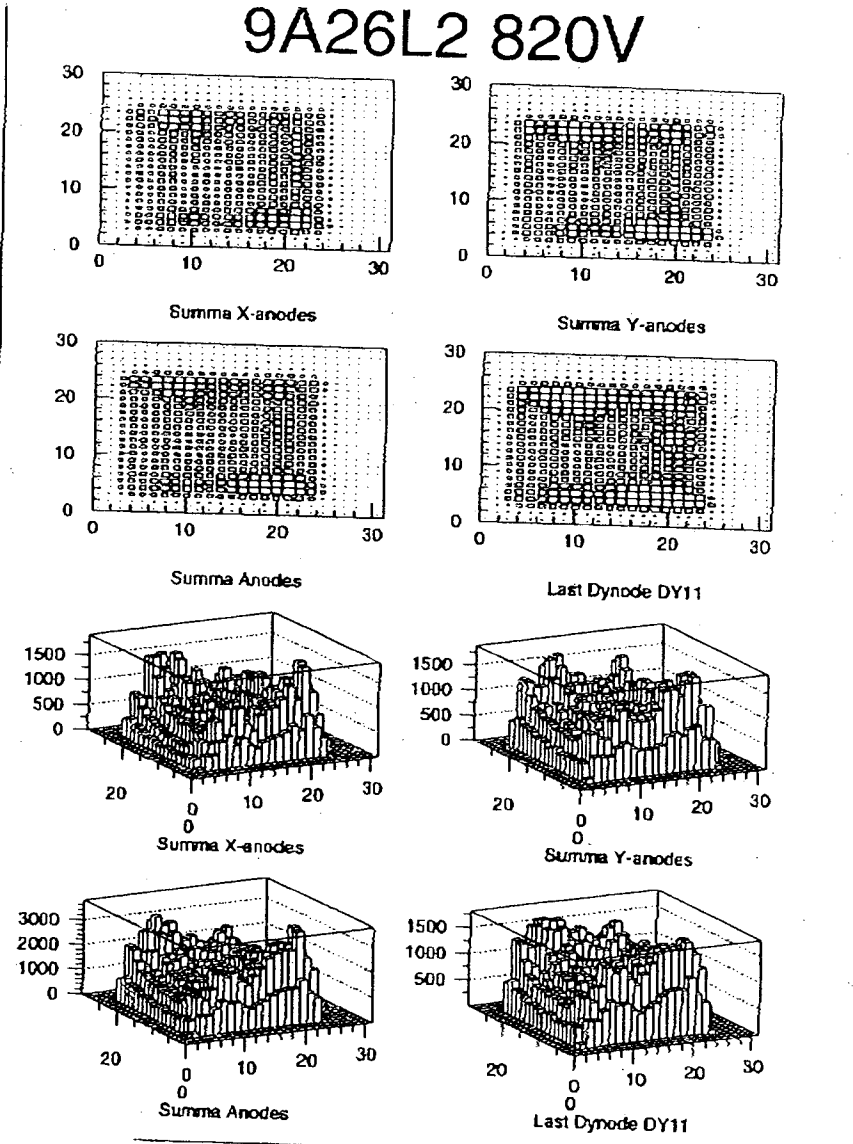

Figure 4: ADC Measurements of the Gain Non-Uniformity for R7600-C12 PMT

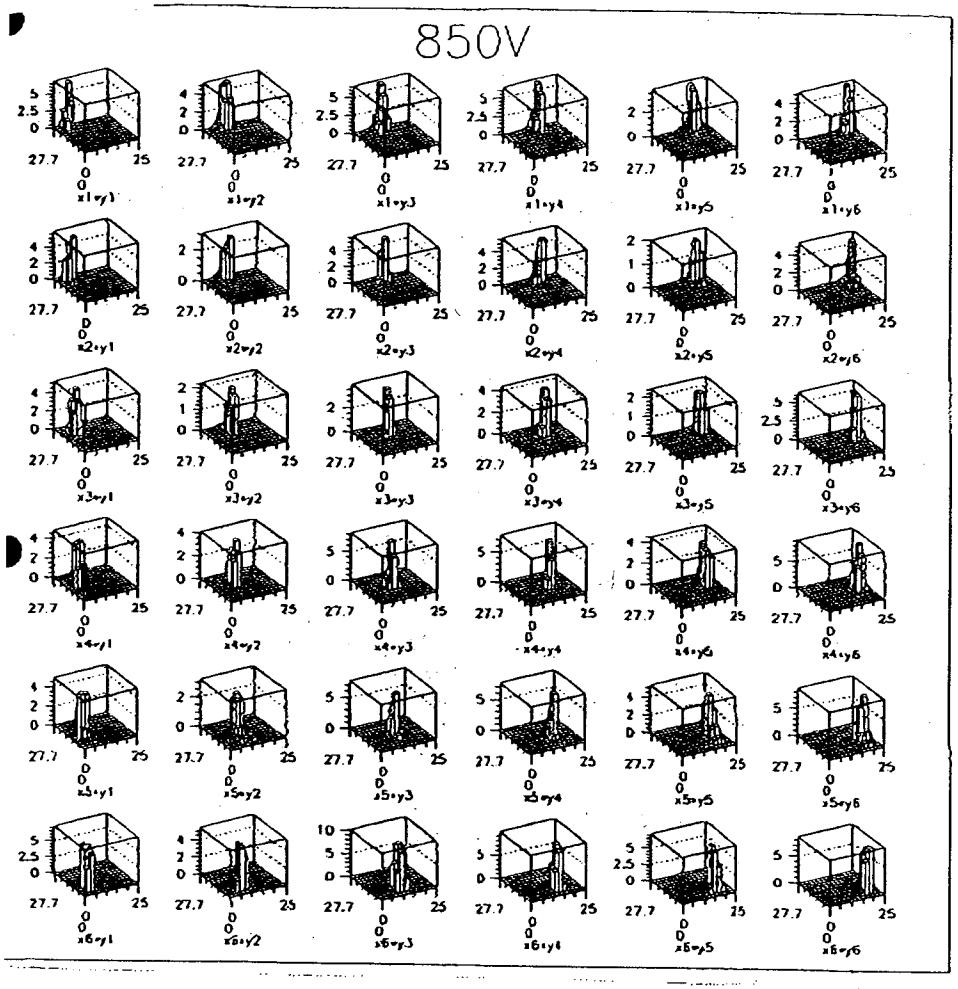

Figure 5: Scan of R7600-C12 PMT using Photon Counting Readout.

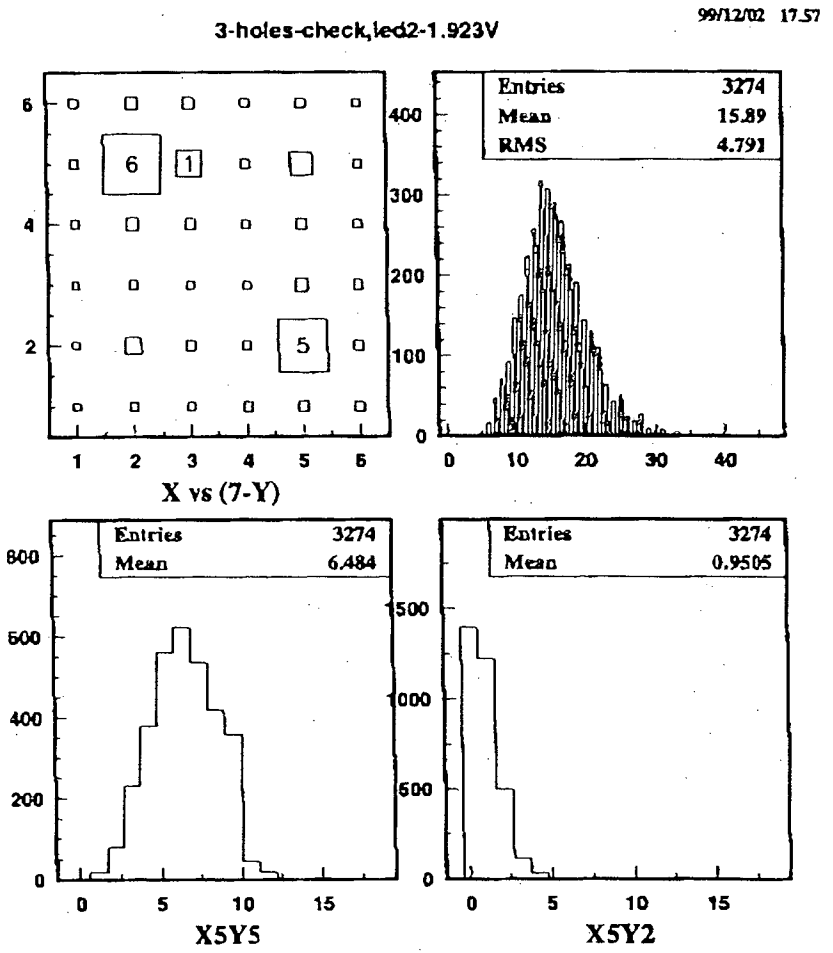

Figure 6: Measured Cross-Talk for R7600-C12 PMT using Photon Counting Readout

Analysis of the photon-counting data and the single-photoelectron gain calibration ADC measurements confirmed that the charge output variation as a function of incident light position primarily corresponds to variations in PMT gain, and not to variations in PMT quantum or collection efficiency. Comparison of the number of photoelectrons measured with ADC readout with the number of counted photoelectrons for the same incident light source level showed the photon counting to be efficient at the level of 80-100% across most of the PMT input area, for the low discriminator threshold which we used. However, these tests also revealed an excess of photoelectrons at late times relative to the incident light pulse – an effect known as afterpulsing. By clamping one x-anode wire discriminator output at a time "on", we were also able to count "singles" on the y-anode wires. We then used an LED-excited fiber to illuminate spots over other anode wires besides that with the clamped output. This test confirmed that discriminated outputs from y-anode wires resulted in coincidences with discriminated x-anode outputs more than 80% of the time. This efficiency was limited by our threshold setting, which in turn was limited by the PMT non-uniformity.

The data collected in the photon counting scans described above was also used to assess the extent of optical and electronic cross-talk between x-y coincidence photon counter channels. When the LED was in a position to provide the maximum efficiency for a given photon counting channel, the average number of photons counted on the other photon counting channels was measured. This evaluation was performed for each of the 6 x 6 photon counting channels, and was performed for a range of LED illumination levels. This last was to assess the rate of random coincidences in our x- and y- wire coincidence photon counting readout method. Two photoelectrons collected in less than the coincidence resolving time (i.e. less than the discriminator output width of 10ns) may generate more than two counts if they arrive on two different x-anodes and two different y-anodes. For ~20 photoelectrons distributed across 1 microsecond (comparable to the rate at which we expect to collect photoelectrons from wavelength-shifting fiber readout) this effect is small, as shown in Figure 6. Nonetheless, the rate of observed cross-talk was greater than that expected from random coincidences. This effect was ultimately traced to the same afterpulsing behavior noted earlier. Afterpulsing had the effect of increasing the apparent discriminator output width, since photoelectrons often resulted in afterpulses near the same crossed-wire location.

We communicated our measurement results to Hamamatsu, and perhaps as a result Hamamatsu has announced that there will be a modified version of the R7600-C12 available starting in summer 2000. It will have a longer photocathode-to-first-dynode distance, which is designed to improve the gain uniformity. It will also have a getter included within the package, to improve the vacuum and eliminate afterpulsing. Other multianode PMTs produced by Hamamatsu (including the R5900-L16 we had used earlier) already include such getters. The previous version of the R7600-C12 (which we tested) will be eliminated. It should be noted that the earlier R7600-C12 was shown to be adequate for our purposes, although the improvements expected from the new R7600-C12 will be useful.

Objective 2: Prototype PET Modules with Photon Counting Electronics

We next constructed photon-counting readout electronics for previously-constructed wavelength-shifting fiber/scintillator prototype detector modules. Since this was a retrofit operation the mechanics were not pretty, but the resulting devices were functionally sound. The modules and their associated readout electronics are shown in Figures 7-10 on the following pages. Two 12cm x 12cm detector modules, each containing 3 layers of CsI(Na) (with each layer 3mm thick) with each module read out by 4 crossed layers of wavelength-shifting fiber, were constructed and tested as shown in Figure 7. Each module contained 4 Anger PMTs that read out the module's fiber/scintillator matrix through a light mixer, as shown in Figure 10. Anode outputs from the Anger PMTs were sent to individual custom gated ADCs, which were read out through our custom PCI interface to a PC operating under LINUX. Dynode outputs from the Anger PMTs were analog summed, shaped, discriminated, and finally used to provide coincidence triggers and subsequent ADC gate signals. Our custom ADCs have internal delay lines so no Anger signals were lost while the triggers were being generated. Wavelength-shifting fibers were routed as shown in Figure 8, with 28mm-wide fiber ribbons multiplexed to 2x14mm strips at the input of each Hamamatsu R5900-L16 PMT. Two such 28mm-wide ribbons were read out from a fiber ribbon layer by two R5900-L16 PMTs, with charge-division Anger coordinates used to demultiplex the fiber coordinate information within a fiber ribbon layer. There were 8 R5900-L16 PMTs read out from each module, providing X-Y gamma-ray interaction coordinate information and allowing depth-of-interaction determination between the 3 scintillator layers. Since the R5900-L16 PMTs do not use crossed-wire anodes, we used simple photon counting rather than the photon-by-photon coincidence method used with the R7600-C12 PMTs. The photon counting readout circuits are shown in Figure 9.

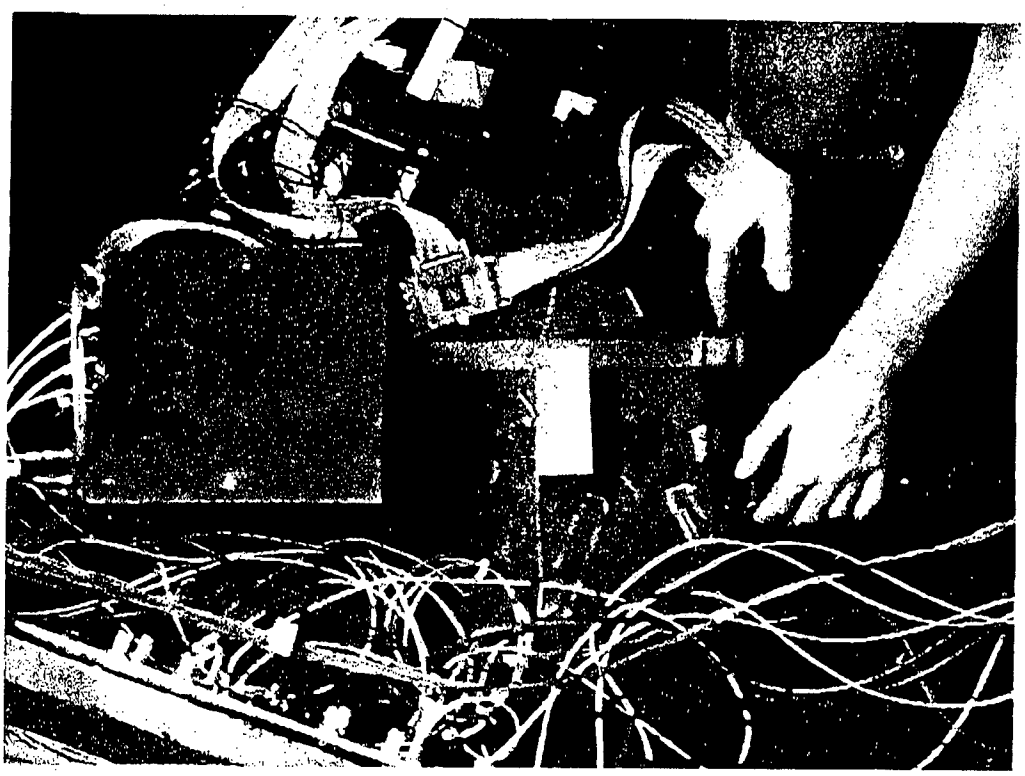

Figure 7: WLS Fiber/Scintillator Prototype Modules under test

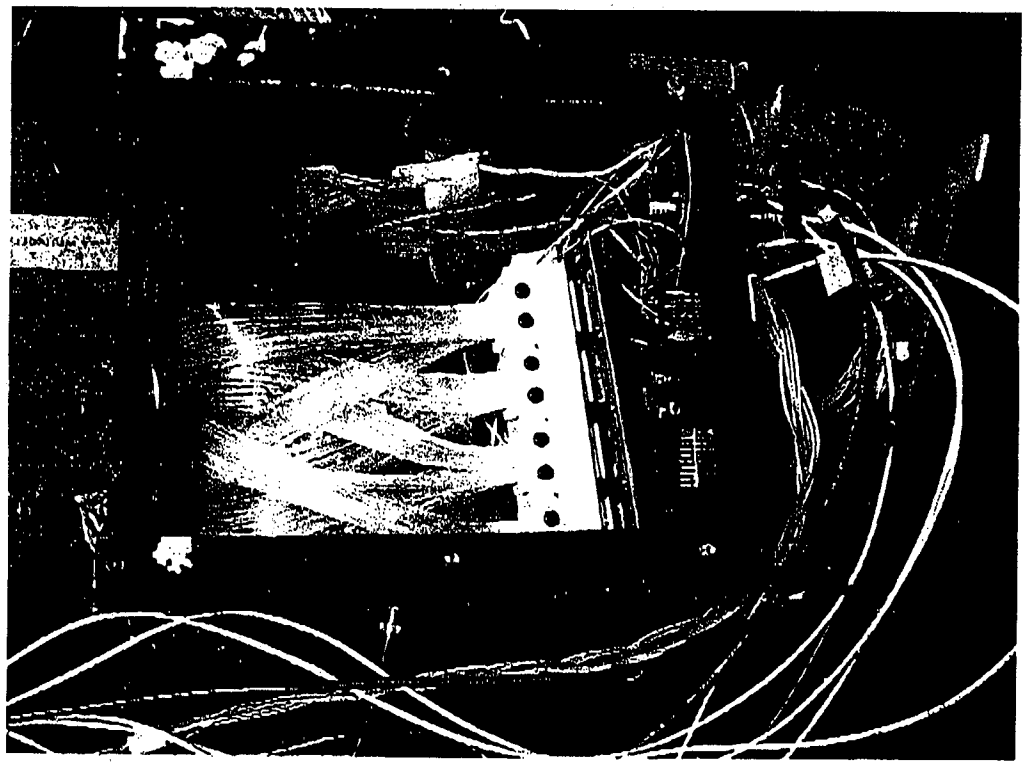

Figure 8: Inside WLS Fiber/Scintillator Prototype Module

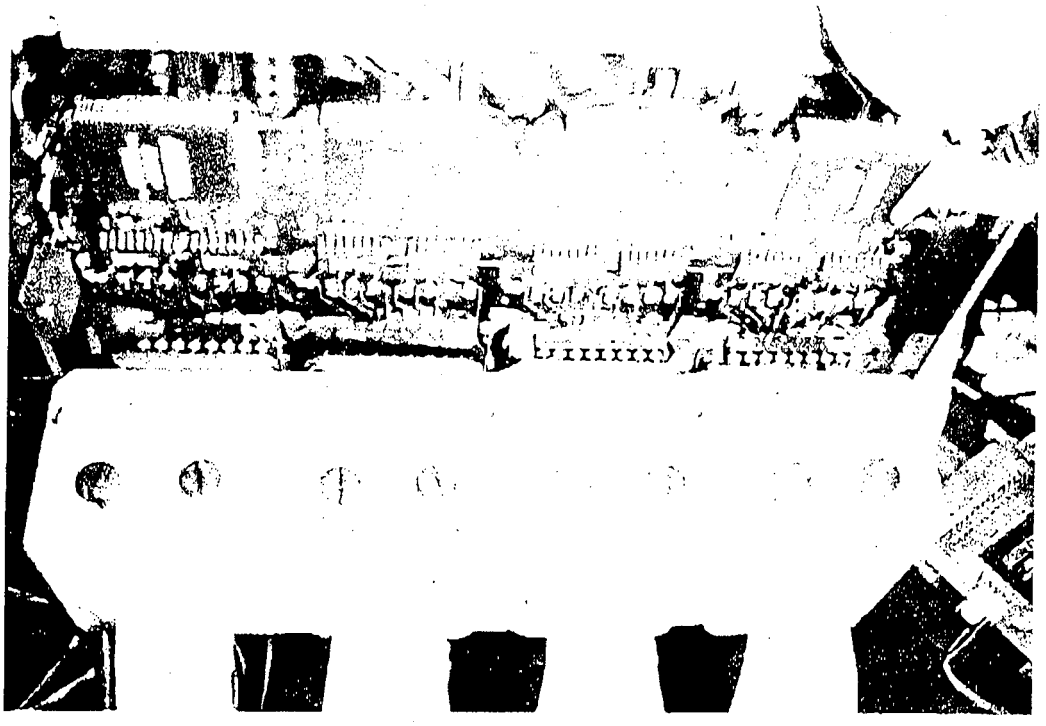

Figure 9: Photon Counting Readout of Hamamatsu R5900-L16 PMTs

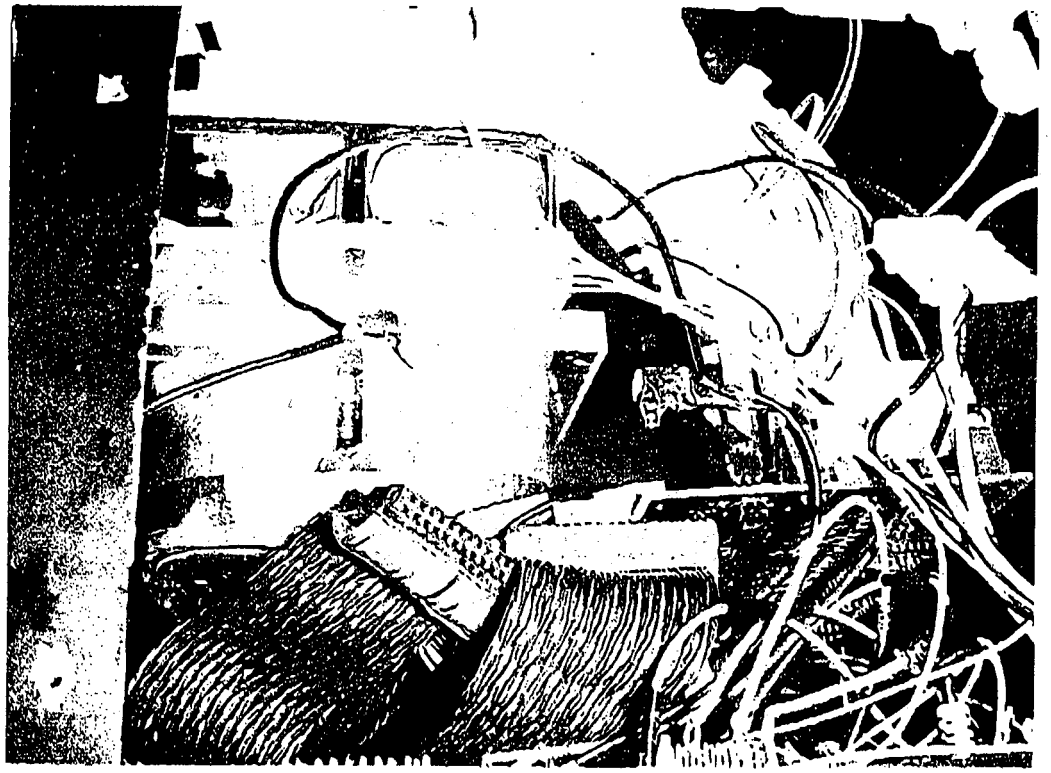

Figure 10: Anger PMTs w/readout, Mixer, Fiber/Scintillator Matrix

Measurements of Prototype Module Performance

Measurements of the performance of the two PET detector modules that have been outfitted with photon counting electronics are still underway. We currently form an event coordinate from the fiber photon counting information with the following algorithm:

- A 3, 4, or 5-anode window (6, 8, or 10mm of fibers) is run across the distribution to find the window location with maximal light collected
- The collected light centroid within the window is calculated
- The light centroid coordinate is linearly mapped into a module coordinate, using a charge division coordinate from the Anger information to demultiplex fiber ribbons read out with common fiber PMTs.

Figure 11 shows the correspondence between the resulting Fiber X vs. Anger X coordinates and Fiber Y vs. Anger Y coordinates for the two modules, with each dot representing a photopeak-photopeak event. The Anger X and Y coordinates are biased toward the center of each module, as expected. Figure 12 shows our spatial resolution for a Na22 point source centered between the two detector modules, with a FWHM of 4.5mm with no rejection of detector Compton scatters. Figure 13 shows the reconstruction of a circulating point source as a uniform circle, while Figure 14 shows the small difference in collected energy for events having different depth-of-interaction in the crystal/fiber layered stack. The spatial resolution we obtain is presently believed to be limited by detector Compton scattering, as discussed below. No spatially-dependent energy correction calibration has been applied, so these are the trigger-level energy distributions.

Effects of Detector Compton Scattering on Spatial Resolution

It should be noted that single-photon counting readout of depth-of-interaction segmented modules offers the potential for discrimination against detector Compton scatter events, at the expense of efficiency. One therefore can measure curves characterizing the module detection efficiency as a function of intrinsic spatial resolution. The photocapture fraction of CsI is 21%, intermediate between that of BGO at 41% and that of NaI at 17%. CsI's density of 4.5 g/cm^3 is also intermediate between BGO's 7.4 g/cm^3 and NaI's 3.7 g/cm^3. CsI has Compton-scatter secondary gammas with roughly twice the range of those in BGO, but with roughly 25% shorter range than those in NaI. When one selects for energy deposition within the photopeak, one invariably selects some events with Compton scatter in the detector, where the secondary gamma ray converted within the same detector block. This forms the "effective photofraction" and is a module geometry- and material-dependent quantity. Since PET detector modules use the total energy deposited to determine the event energy, they also includes detector Compton scatters in their data set when using photopeak-photopeak coincidences. Since we will be recording information as to whether there is energy deposition within more than one depth-of-interaction layer, or whether there was energy deposition at widely separated locations within a given depth-of-interaction layer, we will have an additional handle on rejecting or further processing detector Compton scatter events. Other groups have commented on the possibility of biasing reconstructed interaction positions toward the coordinate-of-first-interaction [9].

We have begun to carry out a detailed Monte Carlo simulation of our current system, and will tune it to match our experimentally measured observations. In addition, an analysis of detector Compton scattering using the Klein-Nishina formula and detector materials properties is being performed as an aid to understanding the data collected from our ~~structured~~ CsI(Na)/WLS fiber assemblies. This effort is ~~already~~ currently underway, yielding the table below comparing detector Compton scatter in BGO, NaI(Tl), and CsI(Na):

Scatter Angle in Degrees	Energy of secondary γ-ray in keV	% of all γ-ray interactions (BGO)	Secondary Range in mm (BGO)	% of all γ-ray interactions (NaI)	Secondary Range in mm (NaI)	% of all γ-ray interactions (CsI)	Secondary Range in mm (CsI)
Photo-capture	--	41	--	17	--	21	--
120-180	0-200	8.5	0.0-1.9	13	0.0-8.3	12	0.0 – 5.8
90-120	200-255	8.5	1.9-3.2	13	8.3-12.9	12	5.8 – 9.2
60-90	255-340	12	3.2-5.6	17	12.9-19.3	16	9.2 – 14.7
30-60	340-440	17	5.6-8.5	22	19.3-25.7	22	14.7 – 20.0
0-30	440-511	13	8.5-10.4	18	25.7-29.2	17	20.0 – 23.1

Illustrations of Module Performance: Figures 11-12.

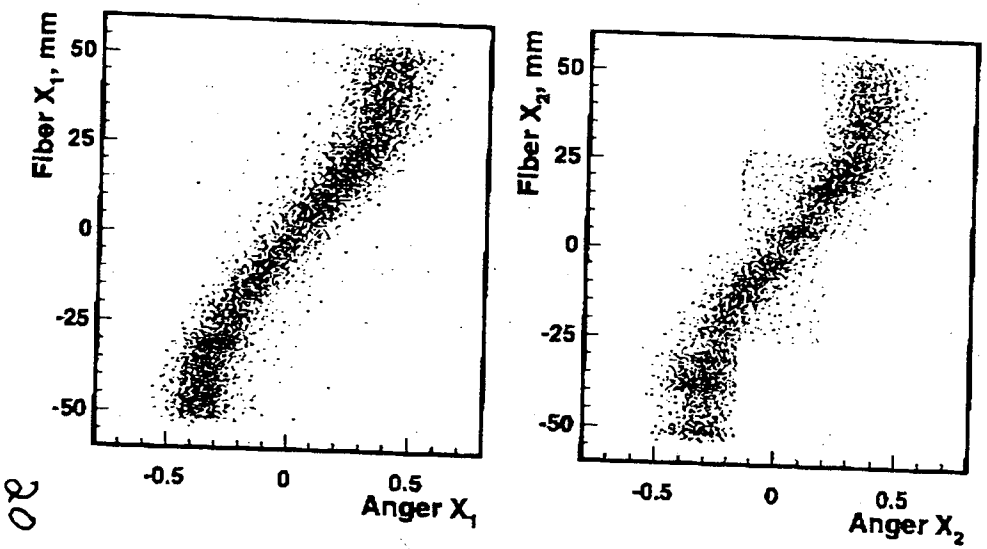

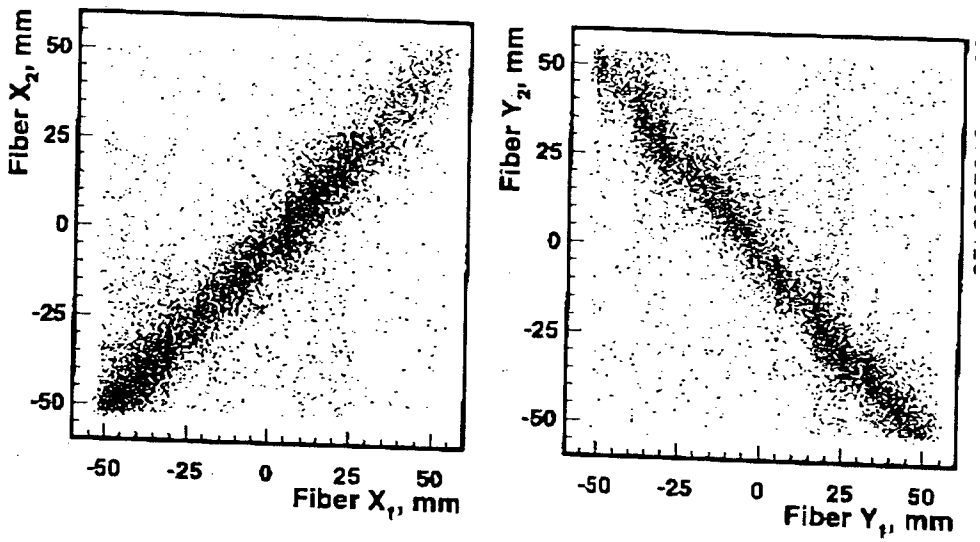

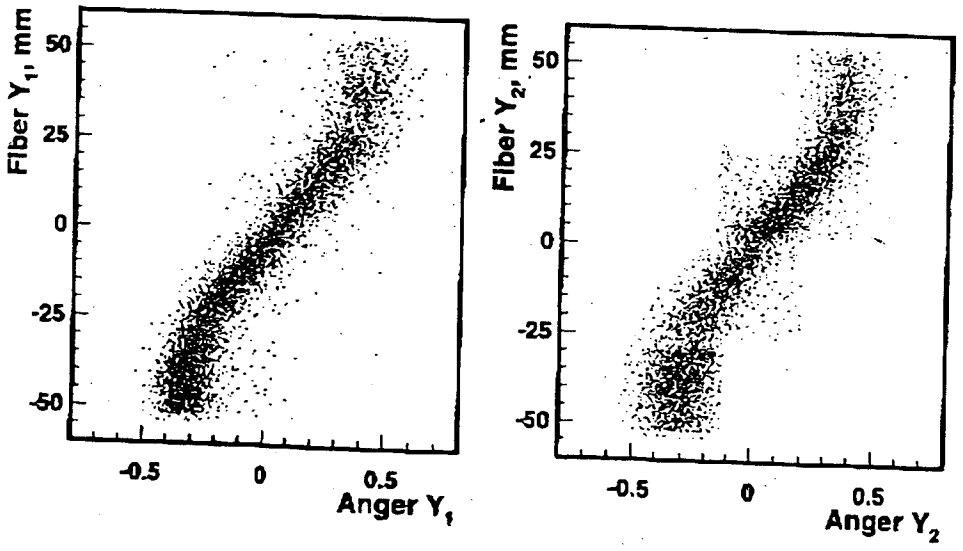

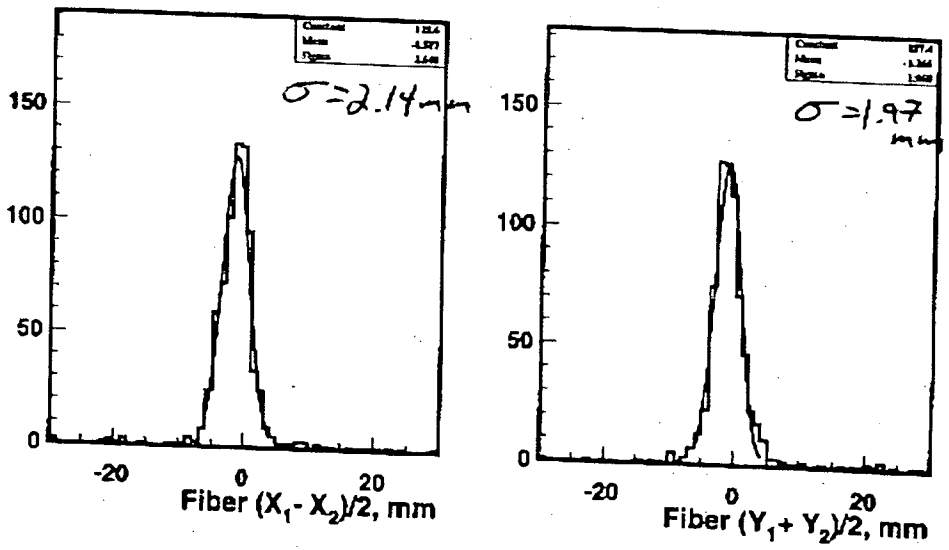

Illustrations of Module Performance: Figures 13-14.

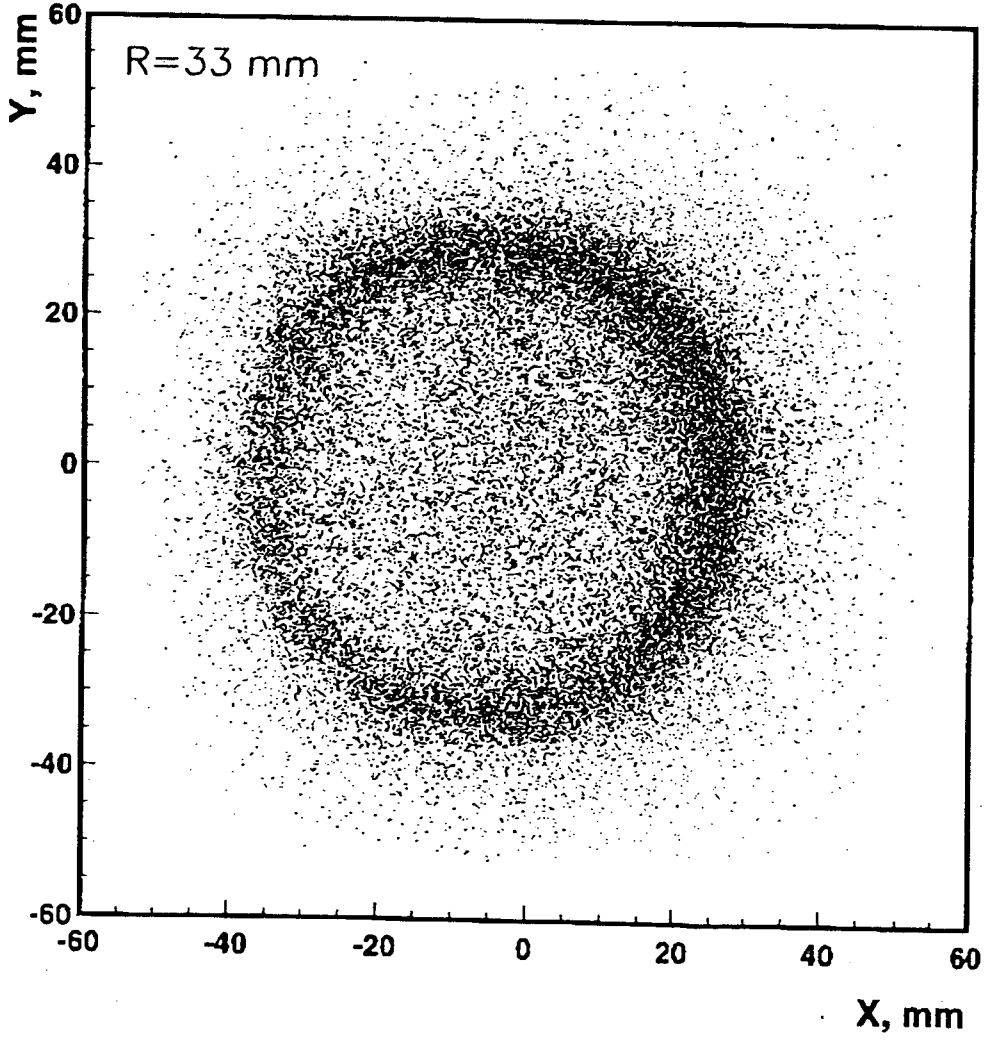

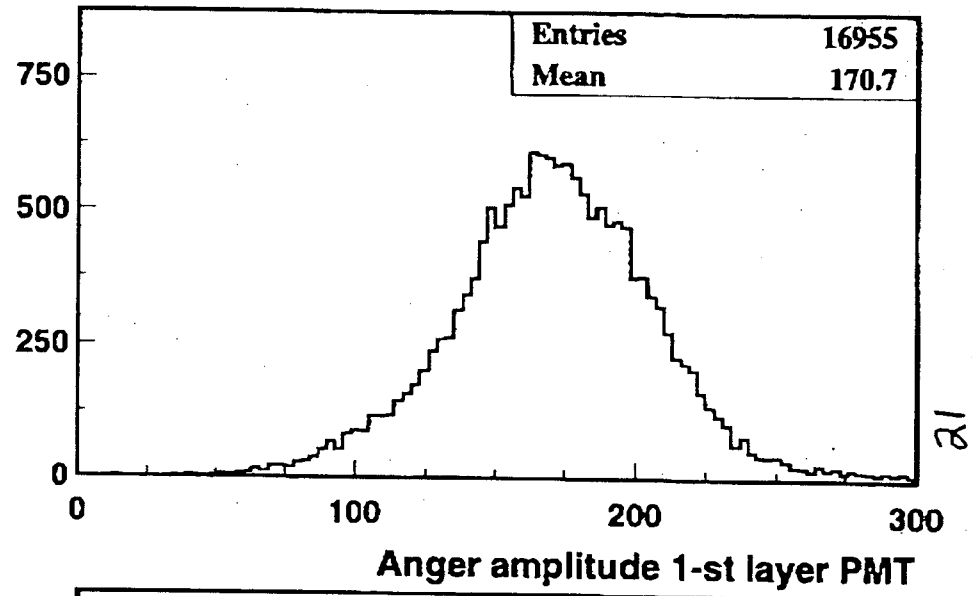

Anger amplitude 1-st layer PMT

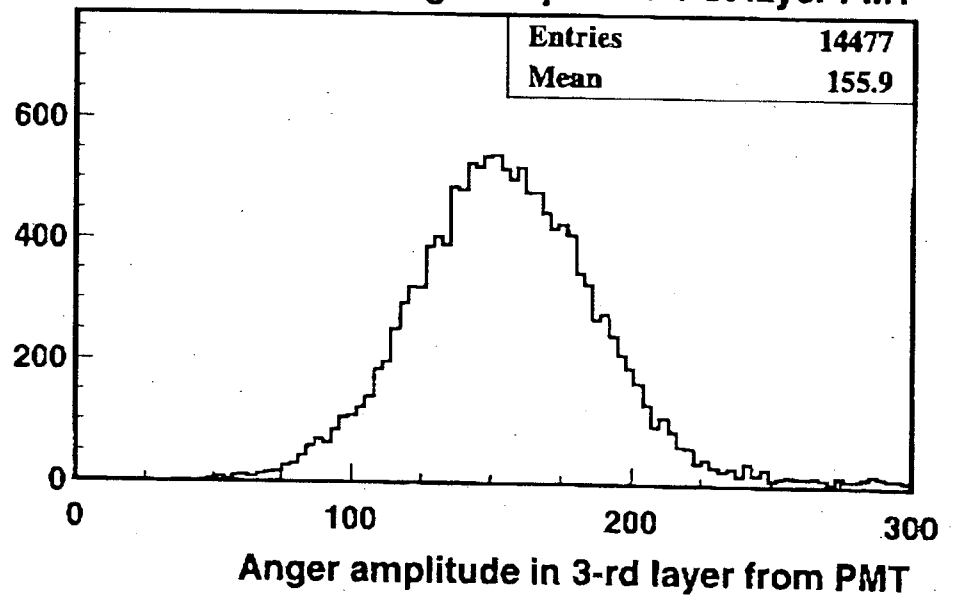

Anger amplitude in 3-rd layer from PMT

Objective 3: System Design, Optimization, and Expected Cost/Performance Analysis

The third objective of our Phase I research program was to generate system performance models which predict the potential capabilities of PET scanner systems incorporating our wavelength-shifting readout technology. As will be discussed in much more detail in the Phase II section of this proposal, the NEMA NU-2 performance standards are typically used to characterize tomograph performance and to comparatively evaluate competing systems. In this section we briefly discuss the most important tomograph performance characteristics, indicate the relative levels of performance of current competing systems, and give results for the expected performance of our proposed system. We begin with a discussion of the basis for the system performance model and the degree to which it has been validated by comparison with measurements performed on actual systems.

The most important tomograph performance parameters (which also hold for coincidence imagers) are:

- Spatial Resolution – the spatial resolving power of the instrument, which is important for detecting and quantitatively measuring activity in small structures
- Sensitivity – the fraction of gamma rays emitted by the patient which are usefully detected by the scanner
- Scatter fraction – the degree to which gamma rays that scatter within the patient are included along with the unscattered gamma rays, contributing to spatially distributed background noise and biasing quantitation
- Rate capability – the degree to which useful gamma rays are collected (rather than lost to acquisition system deadtime) by the system when imaging clinically appropriate amounts of activity, usually expressed as the Noise Equivalent Count Rate (NECR) as a function of activity in the field of view

System spatial resolution is determined by the intrinsic spatial resolution of the detector and several other factors [10]. A block detector will have a FWHM contribution to the width of d/2, which for d=4mm crystals in block detectors starts with just 2.0mm width. This adds in quadrature with a 2.2mm term for block detectors, and also in quadrature with a 1.3mm noncollinearity term and a 0.5mm positron range term for FDG imaging. The resultant is then multiplied by 1.25 due to approximations and errors in the reconstruction process. The result is thus 4.0 mm at best for the best block detectors, and we are getting comparable resolution with our devices. Note that the 2.2mm term includes the effects of detector Compton scatter, and that this effect is larger for the NaI devices. Nonetheless, NaI devices like C-PET and coincidence imagers quote a system reconstructed spatial resolution of <5mm. It is also important to note that this is only at the center of the field of view, and that radial resolution falls to 6mm FWHM 10cm from the center of the FOV, and approaches 8mm FWHM 20cm from the center due to depth-of-interaction effects with the best current scanners. With our depth-of-interaction measurement, we expect to achieve uniform resolution of 4-5mm FWHM throughout the field of view.

For whole-body FDG imaging, the spatial resolution is usually less important than the sensitivity and especially the system rate capability, since the image quality is typically limited by the total event statistics collected. We have calculated our expected system sensitivity for proposed systems using both a simple analytical model [11] and a more detailed Monte Carlo simulation using the SIMSET package [12]. Both methods have been validated by comparison with measurements on actual systems, and the results are shown in Figure 15. The principal factors contributing to the sensitivity are the system geometry and the thickness (stopping power) of the scintillator crystals. We have modeled two systems: the "Surveyor" with 24cm axial field of view, and the "Surveyor-EX" with 36 cm axial field of view. In each case we assume 3.5cm of total CsI(Na) scintillator thickness, with a stopping power of >80%. The large geometric acceptance of the Surveyor-EX pushes its sensitivity beyond that of the best current BGO scanners, while the greater stopping power of its scintillator pushes even the Surveyor sensitivity beyond the C-PET. For comparison, the sensitivity of coincidence imagers can range from 100-200 kcps for the NEMA NU-2.

In addition to the sensitivity, the count rate capability of the detectors is very important. Coincidence imagers in particular have very poor count rate performance, with maximum trues coincidence rates of only a few 10's of kHz for these systems. The C-PET improves upon this through somewhat greater modularity, but it is has lesser modularity than the BGO imagers and subsequently has lower rate capability despite its faster scintillator and narrower coincidence timing window. The typical activity within the patient for a whole-body scan is of order 0.1 uCi/cc, near the middle of the plots shown in Figure 16. Note that the Surveyor-EX has the potential to surpass the BGO systems in useful count rate capability in this regime. This is helped by the lower scatter fraction we expect (calculated using SIMSET) due to the good energy resolution for our high-brightness scintillator (similar to C-PET)

Figure 15: Relative Sensitivity of Current and Proposed Systems.

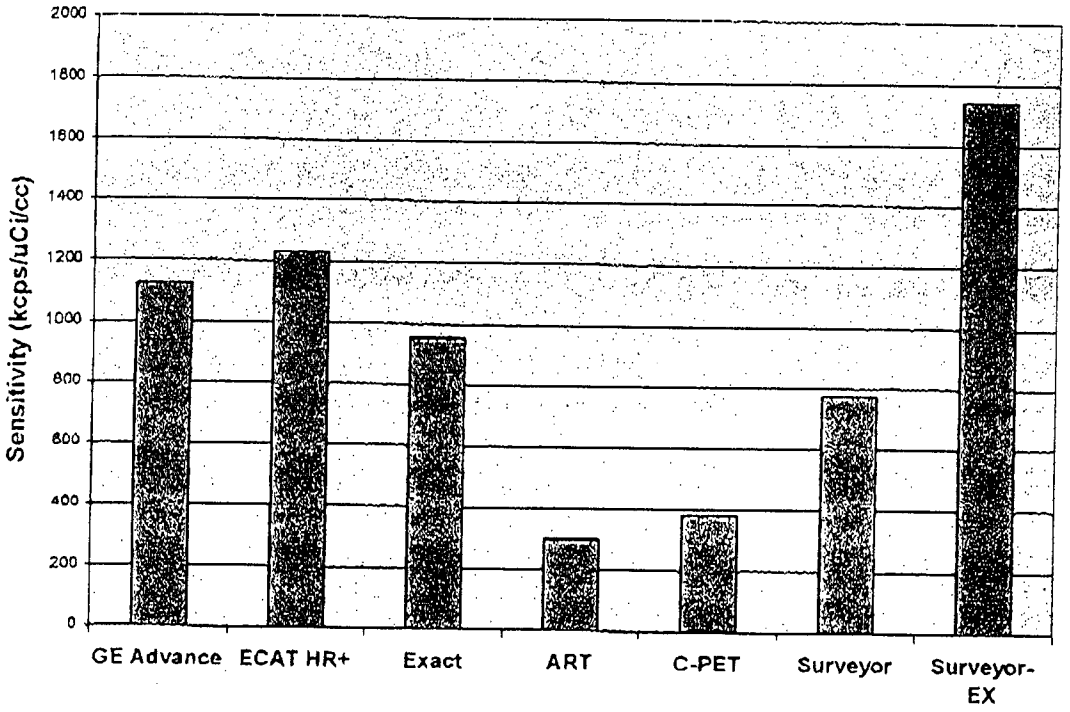

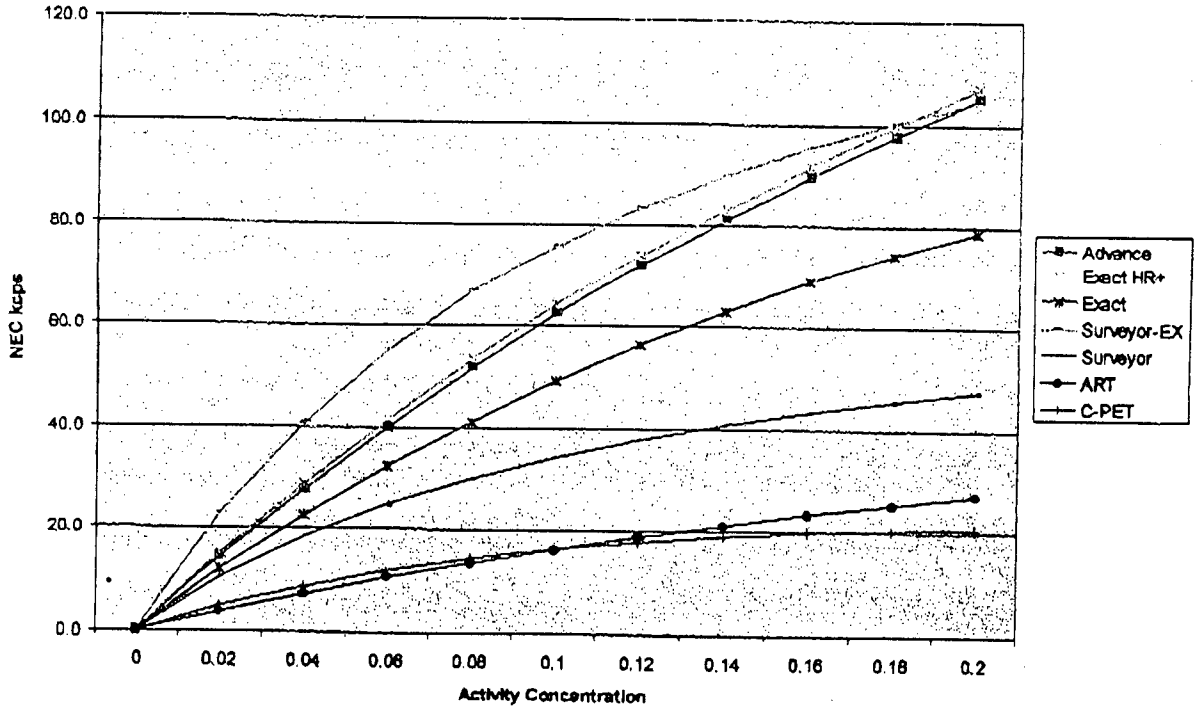

Figure 16: Relative Count Rate Capability of Current and Proposed Systems

The rate capability of the proposed systems have been modelled using methods proposed in the analytical model of Moisan et. al., which has been validated against existing commercial BGO ring systems. In particular, the simple analytical model brings the most pertinent performance issues into sharp relief when implemented as a spreadsheet program, as we have done. One very important parameter for system rate capability is the system singles/trues ratio. It should be noted that the system randoms rate goes like the square of the singles/trues ratio, while it goes only linearly with the timing coincidence window width. Due to the slower decay time of our CsI(Na) scintillator relative to NaI(Tl), we have assumed only a 20ns coincidence window width for CsI(Na) compared to an 8ns coincidence window width used with the C-PET. Nonetheless, because of the much greater stopping power for our thick CsI(Na) crystals we are able to have our randoms=trues rate point higher than for the C-PET, and to have it occur at an activity concentration closer to the clinically relevant regime. Randoms are also quite low for the C-PET in the clinically relevant region, but its high singles rates (due to the high singles/trues ratio) combined with its lesser degree of modularity leads to greater deadtime difficulties. Figure 17 shows the expected trues, randoms, and NEC count rates for the Surveyor-EX system for a simulated NEMA NU-2 rate capability measurement. The livetime fraction is indicated in Figure 18, where we have assumed several electronics readout optimizations which will be described later in the Phase II section.

The simple analytical simulation pointed out the critical role which system modularity and electronics deadtime play in limiting the rate capability for NaI-based and even for BGO-based systems. As will be discussed later, we have assumed 40 x 6 independent trigger modules for the Surveyor-EX system, according to a geometry we will discuss in the Phase II section. By implementing electronics such that they are not paralyzed and can collect a new event while the previous event is being read out, and by not combining modules into "trigger blocks" we expect to be able to keep our trigger-associated live time losses to a minimum. The simulation shown corresponds to what would correspond to a 500-ns paralyzed dead time per module, using the methodology of the Moisan analytic model. We gain more than a factor of two in effective dead time reduction by using non-paralyzable methods, however. We have also not included pile-up rejection methods discussed later in the Phase II section, such as waveform digitization of Anger PMTs and various methods to squeeze extra information out of the fiber signals. For the moment, we have assumed the latter can be used to allow some fiber multiplexing and reduction in the number of fiber readout channels. It is apparent, however, that in the clinically relevant region we have the opportunity to make dead time losses relatively small.

Finally, we have asssessed the cost-of-goods and estimated manufactured cost of our proposed system. There are a number of reasons why we are hopeful that the proposed systems, including even the large-axial-field Surveyor-EX, may have cost-effectiveness advantages relative to the BGO scanners:

- Like the C-PET, we use a scintillator which is considerably less expensive than BGO
- We do not require cutting and polishing of very large numbers of small (4mm x 4mm) crystals
- Like the C-PET, we use larger photomultipliers and fewer readout electronics channels than the BGO block systems
- Like the C-PET, but unlike the coincidence imagers, we do not use a more expensive rotating gantry
- We do not use NaI(Tl), which is sufficiently hygroscopic so as to require special sealing techniques which have resulted in an effective monopoly for a single supplier of NaI to the nuclear medicine market (Bicron)
- We buy our crystals direct from the Ukraine
- Our crystals are soft and easily cut and polished, and simply sealed with an epoxy layer
- Wavelength-shifting fibers are cheap (<$1/m in quantity)
- Our fiber readout electronics is specially designed to be inexpensive
- Our biggest cost-driver is the fiber readout PMTs, and we multiplex the inputs to these heavily. Nonetheless, we are looking to improve on this last and are considering alternative lower-cost photosensors for later developments beyond the proposed Phase II effort.

The system simulations and results we have given here are only intended to be indicative that we are potentially in the right ballpark with our proposed system, and to indicate the types of system design decisions which can have significant impact on system performance. Our overall system simulation plans will be discussed in much greater detail in the Phase II sections which follow later in this proposal. It should be noted, however, that our results are broadly consistent with the contention of Badawi *et al* (from their SIMSET device design study) that the best way to boost PET system clinical performance is to increase the axial field while keeping the system stopping power high. To do this, one needs to use inexpensive materials and techniques such as we have been developing.

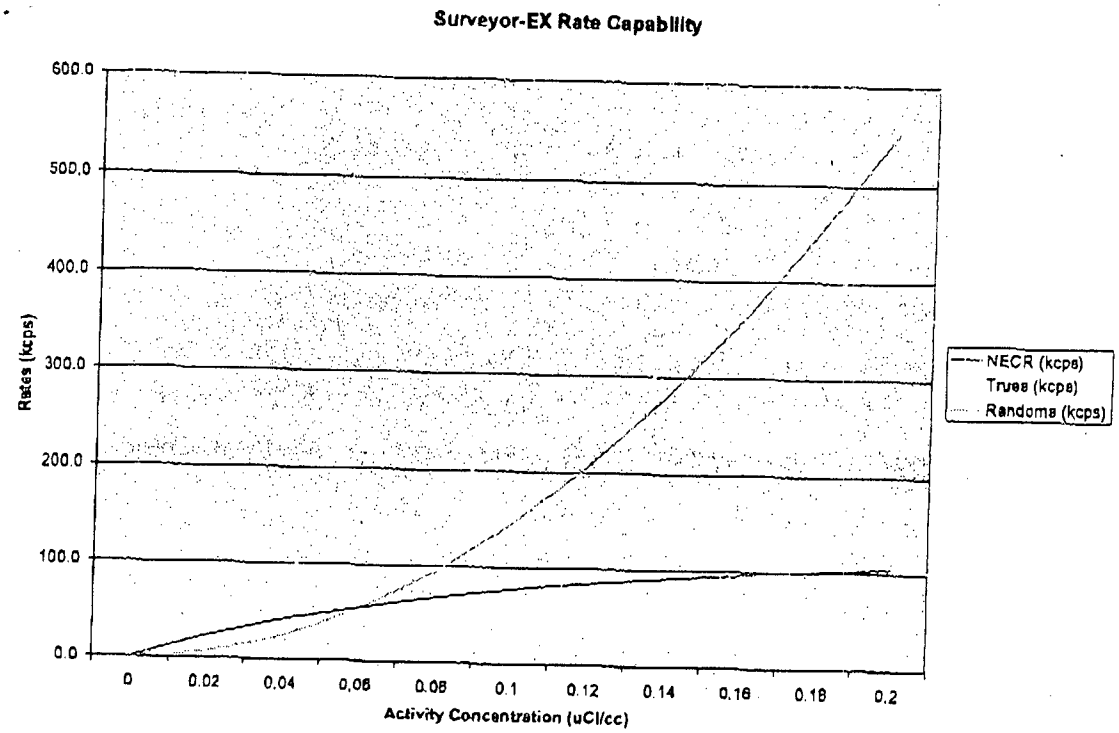

Figures 17: Surveyor-EX NEMA NU-2 Trues, Randoms, and NEC Rate

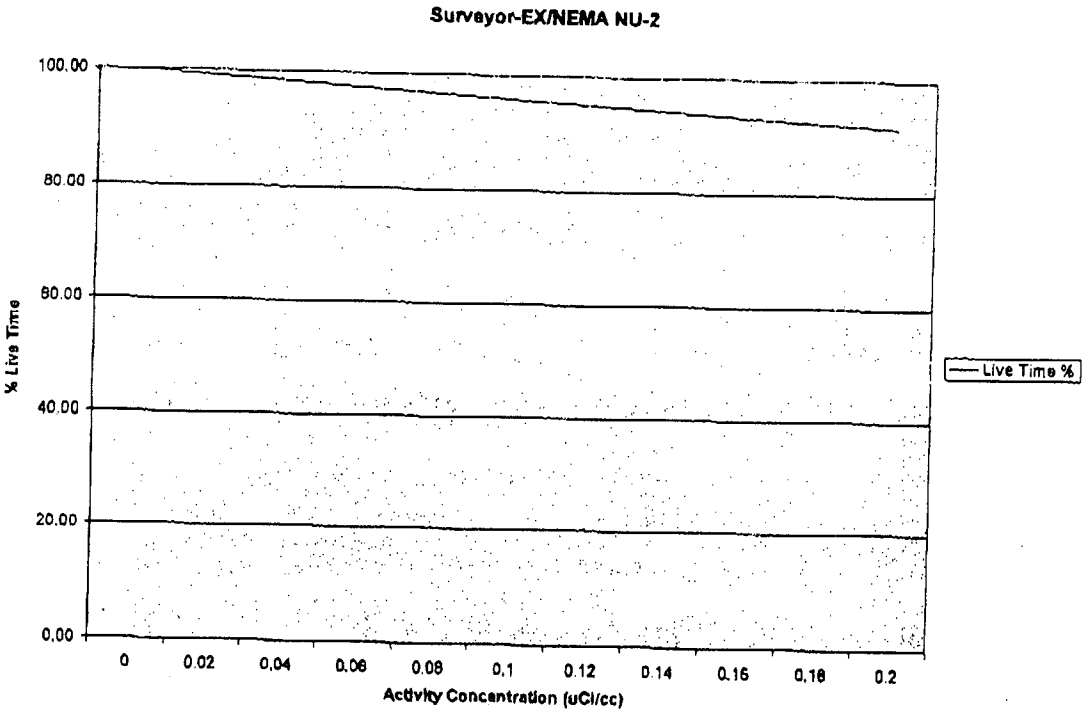

Figures 18: Surveyor-EX NEMA Live Time %